INTERNATIONAL JOURNAL FOR NUMERICAL METHODS IN FLUIDS
Int. J. Numer. Meth. Fluids 2000; **33**: 125–155

Accuracy and stability of a set of free-surface time-domain boundary element models based on B-splines

Bjarne Büchmann*,[1]

Department of Hydrodynamics and Water Resources, Technical University of Denmark, DK-2800 Lyngby, Denmark

SUMMARY

An analysis is given for the accuracy and stability of some perturbation-based time-domain boundary element models (BEMs) with B-spline basis functions, solving hydrodynamic free-surface problems, including forward speed effects. The spatial convergence rate is found as a function of the order of the B-spline basis. It is shown that for all the models examined the mixed implicit–explicit Euler time integration scheme is correct to second order. Stability diagrams are found for models based on B-splines of orders third through to sixth for two different time integration schemes. The stability analysis can be regarded as an extension of the analysis by Vada and Nakos [Vada T, Nakos DE. Time marching schemes for ship motion simulations. In *Proceedings of the 8th International Workshop on Water Waves and Floating Bodies*, St. John's, Newfoundland, Canada, 1993; 155–158] to include B-splines of orders higher than three (piecewise quadratic polynomials) and to include finite water depth and a current at an oblique angle to the model grid. Copyright © 2000 John Wiley & Sons, Ltd.

KEY WORDS: boundary element model; B-splines; higher-order basis functions; stability analysis; three-dimensional; time-domain

1. INTRODUCTION

Boundary element models (BEMs) based on the boundary integral equation method (BIEM) are used in a variety of fields, both in research and in engineering. This paper is devoted to applications with hydrodynamics. Using a frequency domain formulation, a hydrodynamic radiation–diffraction problem with free-surface water waves interacting with a fixed or floating body can be simplified significantly, and thus frequency domain models have been used extensively as tools in engineering to solve time-harmonic linear or weakly non-linear problems. However, in recent years as computer power has increased, BEMs have gained

* Correspondence to: Research Laboratory of Electronics, VLSI Group, MIT Building 36, 8th Floor, 50 Vassar Street, Cambridge, MA 02139-4307, U.S.A.
[1] E-mail: bjarne@buchmann.dk

Received March 1999
Revised July 1999

popularity for time-domain simulations of the three-dimensional hydrodynamic problems encountered in naval architecture and offshore engineering. Even today, though, the time-domain simulation of fully non-linear three-dimensional hydrodynamic free-surface problems tends to be very time consuming (see, e.g. Broeze [1], Celebi *et al.* [2] and Ferrant [3]) and thus perturbation-based time-domain models are often used (see, e.g. Büchmann *et al.* [4] and Kim *et al.* [5]). Consequently, there is a great interest in the understanding and prediction of the accuracy and stability of perturbation-based time-domain BEMs. These predictions are often vital for a successful development of a model. Thus, several authors have described analyses regarding stability, damping and dispersion in the discrete solution obtained in their BEMs, e.g. Bunnik and Hermans [6] and Sierevogel [7]. Even for fully non-linear models, linearized stability analyses are performed (see, e.g. Dommermuth and Yue [8]), since the full system of equations cannot be examined by analytical means. Consequently, the analysis of a linearized model may yield valuable insight also into the behaviour of fully non-linear models.

In the Computer Aided Design (CAD) environment, B-splines are often used as a basis for the computations. The use of B-splines presents a convenient way to define a basis of piecewise polynomial functions. Thus, the functions described by B-splines are also piecewise polynomial in nature. Among the attractive features of B-splines is a local support, i.e. that each basis function is non-zero only in a small part of the computational domain. Also, spatial derivatives can be obtained accurately through analytical differentiation of the basis functions. This last property is especially advantageous when spatial derivatives on curved surfaces are needed, such as when the pressure forces on a body are evaluated in a radiation–diffraction problem. Today, B-splines or other polynomials are used as basis functions in BEMs, both in frequency domain models (e.g. Harten and Efrony [9] and Maniar [10]), perturbation-based time-domain models (e.g. Kring [11] and Nakos [12]) and in models for fully non-linear three-dimensional calculations (e.g. Kim and Kim [13]). A stability analysis for a deep-water time-domain BEM based on third-order B-splines was given by Vada and Nakos [14] using the assumption that a current and the model grid are collinear, i.e. that a current does not intersect the model grid at an oblique angle. More details of the calculations performed are given by Vada [15]. However, for problems involving bluff bodies and low speed of the body or a weak current, the angle between the grid and the local underlying current may well be rather large. The results given in the present work can be regarded as an extension of the work of Vada and Nakos [14] to include higher-order B-splines, finite water depth and an arbitrary angle between the underlying current and the model grid.

2. GOVERNING EQUATIONS AND BOUNDARY CONDITIONS

A three-dimensional irrotational flow in a homogeneous, incompressible and inviscid fluid is considered. t denotes time and $\mathbf{x} = (x, y, z)$ is the position vector. Then a velocity potential $\phi(\mathbf{x}, t)$ can be defined so that the velocity $\mathbf{u}$ in the three spatial dimensions can be written as

$$\mathbf{u} = \nabla\phi = (\phi_x, \phi_y, \phi_z) \tag{2.1}$$

where ∇ is the gradient operator and the subscripts x, y and z denote the spatial derivatives in the respective directions. The co-ordinate system is chosen such that $z = 0$ corresponds to the still water level. The continuity equation combined with the condition of an irrotational flow yields the well-known Laplace equation

$$\nabla^2 \phi = 0 \tag{2.2}$$

The Laplace equation is the governing differential equation in the fluid domain bounded by a horizontal sea bed and a free surface (Figure 1). For the analysis presented in this work it is assumed that the fluid extends to infinity in all horizontal directions.

For the free surface, two non-linear boundary conditions are given. The kinematic free-surface boundary condition is

$$n_t - \phi_z + \phi_x \eta_x + \phi_y \eta_y = 0, \quad \text{at } z = n \tag{2.3}$$

where η is the elevation of the free surface and the subscript t denotes the partial derivative in time. The dynamic free-surface boundary condition is given by the Bernoulli equation

$$\phi_t + g\eta + \frac{1}{2}|\nabla \phi|^2 = 0, \quad \text{at } z = \eta \tag{2.4}$$

where g is the acceleration due to gravity, and the pressure is assumed to be constant on the free surface and thus can be omitted. The horizontal sea bed at the depth h is considered to be impermeable, and thus the velocity component perpendicular to the sea bed is zero,

$$\phi_z = 0, \quad \text{at } z = -h \tag{2.5}$$

The kinematic and dynamic boundary conditions (2.3) and (2.4) can be linearized using Taylor expansion and perturbation expansion techniques. The free-surface conditions for linear waves riding on a uniform (zeroth-order) current, $\nabla \phi^{(0)} = (U, V, 0) = \mathbf{U}$, take the form

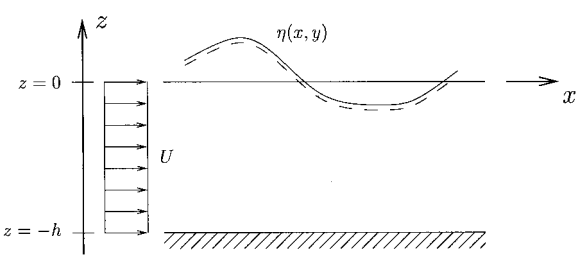

Figure 1. Definition of fluid domain and boundaries. Note that the problem set-up is in three spatial dimensions, even though only two are shown here.

$$\eta_t^{(1)} = \phi_n^{(1)} - U\eta_x^{(1)} - V\eta_y^{(1)}, \quad \text{at } z = 0 \tag{2.6}$$

$$\phi_t^{(1)} = -g\eta^{(1)} - U\phi_x^{(1)} - V\phi_y^{(1)}, \quad \text{at } z = 0 \tag{2.7}$$

where the superscript (1) denotes a first-order quantity. Since no higher-order effects will be discussed here, these superscripts are omitted in the remaining part of this work. Subscript n denotes partial differentiation along a unit normal vector pointing outwards from the fluid domain. On the linearized free surface $\phi_n = \phi_z$, however, the subscript n is preferred to emphasize the connection with the boundary integral equation (see below). Earlier works, such as Büchmann *et al.* [4], can be consulted for a more detailed description of the mathematical background.

When Green's second identity is used, the governing equation (2.2) in the linearized fluid domain ($-h \le z \le 0$) is transformed into a boundary integral equation of the form

$$2\pi\phi(\mathbf{x}) = \iint_{\Gamma(\xi)} \phi_n(\boldsymbol{\xi}) G(\mathbf{x}, \boldsymbol{\xi})\, \mathrm{d}\Gamma - \iint_{\Gamma(\xi)} \phi(\boldsymbol{\xi}) G_n(\mathbf{x}, \boldsymbol{\xi})\, \mathrm{d}\Gamma \tag{2.8}$$

where Γ denotes the boundary over which the integration is to be performed. In Equation (2.8) $\boldsymbol{\xi} = (\xi_1, \xi_2, \xi_3)$ is an integration point on the boundary of the domain and $\mathbf{x} = (x, y, z)$ is a field point. In order to avoid integration over the sea bed, the Green's function G is chosen as

$$G(\mathbf{x}, \boldsymbol{\xi}) = \frac{1}{r} + \frac{1}{r'} \tag{2.9}$$

i.e. as a Rankine source and mirror terms, where

$$r = \sqrt{(x - \xi_1)^2 + (y - \xi_2)^2 + (z - \xi_3)^2} \tag{2.10a}$$

$$r' = \sqrt{(x - \xi_1)^2 + (y - \xi_2)^2 + (z + \xi_3 + 2h)^2} \tag{2.10b}$$

Thus, the integration in Equation (2.8) is performed only over the linearized free surface ($\xi_3 = 0$). This means that in (2.8), ϕ_n can be replaced by ϕ_z. Also, since all the field points will be located on the free surface ($z = 0$), the Green's function can then be written as a function of $\mathbf{x} - \boldsymbol{\xi} = \mathbf{r} = (r_1, r_2, 0)$

$$G(\mathbf{x}, \boldsymbol{\xi}) = G(\boldsymbol{x} - \boldsymbol{\xi}) = G(\mathbf{r}) = \frac{1}{\sqrt{r_1^2 + r_2^2}} + \frac{1}{\sqrt{r_1^2 + r_2^2 + 4h^2}}, \quad \text{for } z = \xi_3 = 0 \tag{2.11}$$

Generally, in a BEM some set of basis functions (or shape functions) is defined, such that the unknowns at a given time step, rather than being the 'physical' parameters (ϕ, ϕ_n, η) in the problem, are the coefficients with which each of the basis functions contributes to the total solution. Often a collocation approach is taken when defining a set of collocation points (or 'nodes') in which the boundary integral equation and the boundary conditions are satisfied. In each time step of the model a mixed set of equations is solved, first by time integrating the

boundary conditions, and subsequently by solving the boundary integral equations, typically a large dense linear system, to obtain the remaining unknowns (see Bühmann *et al.* [4] for more details).

3. B-SPLINE BASIS IN BEMs

One of the largest problems using BEMs is that in general the CPU time and memory requirements needed to solve a problem increase rapidly with the number of unknowns in the problem. Typically, the memory requirement will be around $O(N^2)$, where N is the number of unknowns. Similarly, the CPU time requirement varies from $O(N^2)$ to $O(N^3)$ depending on which method is used for solving the linear system (the boundary integral equations). Today several different techniques can be used to accelerate BEMs. When piecewise constant basis functions are chosen, it is possible to speed up the process significantly. If multipole or pre-corrected FFT accelerated iterative techniques (see, e.g. Korsmeyer *et al.* [16] and Nabors *et al.* [17]) are used, problems requiring in the order of 10^5 panels (and unknowns) can be solved within a reasonable time. Alternatively, a significant speedup can be gained by using a domain-decomposition approach (see, e.g. Harten and Efrony [9], de Haas [18] and Wang *et al.* [19]). The last two of these domain-decomposition methods yield BEMs where fully non-linear problems with the order of 10^3–10^4 unknowns have been solved.

While both the sparsification algorithms (multipole and pre-corrected FFT accelerated iterative techniques) and the domain-decomposition technique aim at reducing the cost per unknown in the model, the B-spline basis approach aims at improving the accuracy obtained per unknown in the model. Obviously, when a piecewise constant set of basis functions is used, a lot of unknowns are needed to resolve even a smooth function. Thus, better basis functions are needed. Since the velocity potential is a rather smooth function in space (the gradient of the potential is the local velocity), the potential may be approximated to a high accuracy by using a piecewise polynomial basis. Thus, a set of basis functions where each basis function is piecewise polynomial is constructed—the B-spline basis. It should be noted that B-splines and non-uniform rational B-splines (NURBS) today are widely used in both CAD and computer visualization for designing curves and surfaces [20]. Thus, it would be a great advantage for a BEM if the program could interpret geometrical data in a B-spline format. Then, the complex surfaces needed for the modelling could be generated by using an existing CAD tool, and the need for tedious grid generation could be avoided. The choice to use B-splines also for the basis functions in the BEM is then straightforward.

In his frequency domain BEM, Maniar [10] used a B-spline basis to get spatial convergence rates increasing with the order of the B-spline basis. Also, it was noted by Maniar that to obtain a 1.0–0.1 per cent accuracy, 10–60 times fewer unknowns are needed when using a B-spline method than when using a constant panel method. For smaller relative errors it will be even more advantageous to use a method based on B-splines.

The properties of B-splines can be found in textbooks (e.g. Schumaker [21]). In this work, $N^{(m)}(x)$ will denote a normalized B-spline centred on $x = 0$ and defined on a uniform grid with mesh size Δx. The size of the support of $N^{(m)}$ (the domain on which the function is non-zero) is then $m\Delta x$. The shape of these B-splines on a uniform grid is shown in Figure 2.

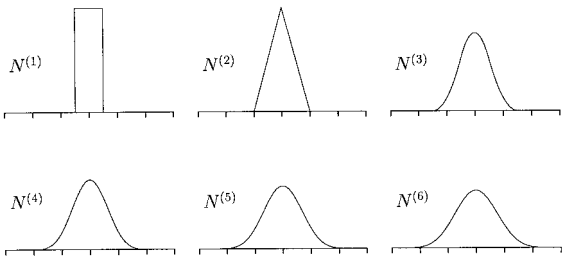

Figure 2. One-dimensional B-spline basis functions of orders one through six. The B-splines have been normalized such that the integral value is kept constant.

When the convolution properties of the B-splines are used, it can be shown that the continuous Fourier transform of the (normalized) B-spline, $N^{(m)}(x)$, is

$$\tilde{N}^{(m)}(u) = \left(\frac{\sin(u\Delta x/2)}{u\Delta x/2}\right)^m \tag{3.1}$$

See Appendix A for the Fourier transform definitions and notations used in this work. Similarly, by defining a two-dimensional basis function as a product of two B-splines

$$N^{(m)}(x, y) = N^{(m)}(x)N^{(m)}(y) \tag{3.2}$$

the continuous Fourier transform becomes

$$\tilde{N}^{(m)}(u, v) = \left(\frac{\sin(u\Delta x/2)}{u\Delta x/2}\right)^m \left(\frac{\sin(v\Delta y/2)}{v\Delta y/2}\right)^m \tag{3.3}$$

4. THE LINEAR CONTINUOUS DISPERSION RELATION

A free surface of infinite extent over a finite water depth is considered. The linearized equations for waves riding on a uniform (zeroth-order) current are Equations (2.6)–(2.8). Taking the continuous Fourier transform in time (sub-tilde) and space of the two free-surface boundary conditions (2.6) and (2.7) yields directly

$$\mathrm{i}(\omega - Uu - Vu)\tilde{\underset{\sim}{\eta}} = \tilde{\underset{\sim}{\phi}}_z \tag{4.1}$$

$$\mathrm{i}(\omega - Uu - Vv)\tilde{\underset{\sim}{\phi}} = -g\tilde{\underset{\sim}{\eta}} \tag{4.2}$$

Note that the Fourier transform definitions used here and in the following are defined in detail in Appendix A. The variables u and v are respectively the x and y components of the wavenumber vector, $\boldsymbol{\kappa} = (u, v)$. The wavenumber κ is then found as $\kappa = |\boldsymbol{\kappa}| = \sqrt{u^2 + v^2}$. ω is the cyclic frequency and i is the imaginary unit.

For field and integration points both on the free surface, the Green's function has the form (2.11). In this case, taking the continuous Fourier transform in time and space of the boundary integral equation (2.8) yields

$$\begin{aligned}2\pi\tilde{\phi}(u,v;\omega) &= \int_{-\infty}^{\infty}\left[\iiint_{-\infty}^{\infty}\iint_{\Gamma(\xi)}\phi_z(\boldsymbol{\xi})G(\mathbf{x}-\boldsymbol{\xi})\exp(\mathrm{i}ux+\mathrm{i}vy)\,\mathrm{d}\Gamma\,\mathrm{d}x\,\mathrm{d}y\right]\exp(-\mathrm{i}\omega t)\,\mathrm{d}t\\ &\quad-\int_{-\infty}^{\infty}\left[\iiint_{-\infty}^{\infty}\iint_{\Gamma(\xi)}\phi(\boldsymbol{\xi})G_n(\mathbf{x}-\boldsymbol{\xi})\exp(\mathrm{i}ux+\mathrm{i}vy)\,\mathrm{d}\Gamma\,\mathrm{d}x\,\mathrm{d}y\right]\\ &\quad\times\exp(-\mathrm{i}\omega t)\,\mathrm{d}t\\ &= \int_{-\infty}^{\infty}\tilde{\mathscr{F}}[(\phi_z\otimes G)(\mathbf{x})]\exp(-\mathrm{i}\omega t)\,\mathrm{d}t-\int_{-\infty}^{\infty}\tilde{\mathscr{F}}[(\phi\otimes G_n)(\mathbf{x})]\exp(-\mathrm{i}\omega t)\,\mathrm{d}t\end{aligned} \tag{4.3}$$

where the two-dimensional continuous convolution product operator $\otimes$ is defined in Appendix A. Using the Fourier transform of a continuous convolution product this equation is reduced to

$$\begin{aligned}2\pi\tilde{\phi}(u,v;\omega) &= \int_{-\infty}^{\infty}\tilde{\phi}_z(u,v;t)\tilde{G}(u,v)\exp(-\mathrm{i}\omega t)\,\mathrm{d}t\\ &\quad-\int_{-\infty}^{\infty}\tilde{\phi}(u,v;t)\tilde{G}_n(u,v)\exp(-\mathrm{i}\omega t)\,\mathrm{d}t\\ &= \tilde{\phi}_z(u,v;\omega)\tilde{G}(u,v)-\tilde{\phi}(u,v;\omega)\tilde{G}_n(u,v)\end{aligned} \tag{4.4}$$

Combining Equations (4.1), (4.2) and (4.4) and remembering that $(u,v)=\boldsymbol{\kappa}$ gives

$$[g(2\pi+\tilde{G}_n)-(\omega-\boldsymbol{\kappa}\cdot\mathbf{U})^2\tilde{G}]\tilde{\phi}=0 \tag{4.5}$$

yielding a continuous dispersion relation of the form

$$W(\omega,\boldsymbol{\kappa},\mathbf{U})\equiv g\frac{2\pi}{\tilde{G}}\left(1+\frac{\tilde{G}_n}{2\pi}\right)-(\omega-\boldsymbol{\kappa}\cdot\mathbf{U})^2=0 \tag{4.6}$$

On the linearized free surface ($z=0$) the Fourier transforms of $G(\mathbf{x})$ and $G_n(\mathbf{x})$ are needed. Note that on the free surface the Green's function, (2.9)–(2.10) and its normal derivative can be written as

$$G(\mathbf{x})=\frac{1}{\sqrt{x^2+y^2}}+\frac{1}{\sqrt{x^2+y^2+4h^2}},\quad\text{for } z=0 \tag{4.7a}$$

$$G_n(\mathbf{x}) = G_z(\mathbf{x}) = \frac{-2h}{(x^2+y^2+4h^2)^{3/2}}, \quad \text{for } z = 0 \tag{4.7b}$$

Through direct integration using, for example, the integration tables in Gradshteyn and Ryzhik [22], it can be shown after some calculations, that the continuous Fourier transforms (in space) of $G(\mathbf{x})$ and $G_n(\mathbf{x})$ are

$$\tilde{G}(u, v) = \frac{2\pi}{\sqrt{u^2+v^2}}(1 + \exp(-2h\sqrt{u^2+v^2})) = \frac{2\pi}{\kappa}(1 + \exp(-2\kappa h)) \tag{4.8a}$$

$$\tilde{G}_n(u, v) = -2\pi \exp(-2h\sqrt{u^2+v^2}) = -2\pi \exp(-2\kappa h) \tag{4.8b}$$

Inserting these into (4.6) yields

$$g\kappa \tanh \kappa h - (\omega - \boldsymbol{\kappa}\cdot\mathbf{U})^2 = 0 \tag{4.9}$$

which is the well-known continuous dispersion relation for linear waves riding on a uniform current in finite water depth.

5. THE DISCRETE DISPERSION RELATION

For the analysis made here, a free surface of infinite extent is considered, and thus an infinite number of basis functions is used to describe the 'physical' parameters on the surface. Each basis function is based on (normalized) B-splines, and a linear combination of all the basis functions is used to describe each variable, i.e.

$$\phi(\mathbf{x}, t) = \sum_{j=-\infty}^{\infty} a_j(t) B_j^{(m)}(\mathbf{x}) \tag{5.1a}$$

$$\phi_z(\mathbf{x}, t) = \sum_{j=-\infty}^{\infty} b_j(t) B_j^{(m)}(\mathbf{x}) \tag{5.1b}$$

$$\eta(\mathbf{x}, t) = \sum_{j=-\infty}^{\infty} c_j(t) B_j^{(m)}(\mathbf{x}) \tag{5.1c}$$

As mentioned in Section 3, the superscript (m) denotes the order of the B-splines. A uniform rectangular grid with grid spacings Δx and Δy is defined on the free surface. Similarly, a temporal discretization with a constant time step size Δt is used. Due to the uniform rectangular grid any basis function $B_j^{(m)}$ can be related to one basis function at the origin (see Figure 3) as

$$B_j^{(m)}(\mathbf{x}) = N^{(m)}(\mathbf{x} - \mathbf{x}_j) \tag{5.2}$$

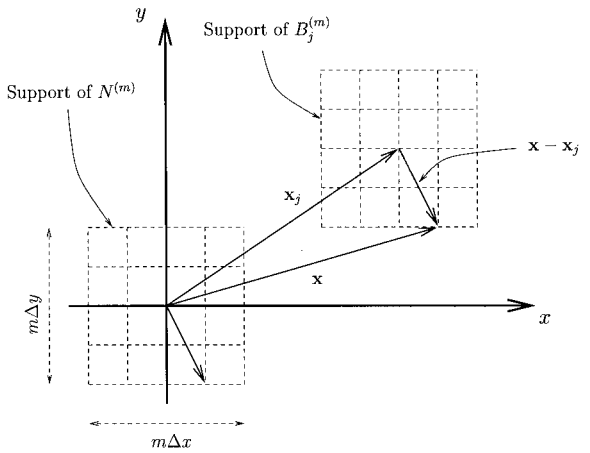

Figure 3. Translation of an arbitrary basis function $B_j^{(m)}(\mathbf{x})$ to a basis function $N^{(m)}(\mathbf{x} - \mathbf{x}_j)$ with centre at the origin.

Since the coefficients (a_j, b_j, c_j) of the basis functions may be regarded as discrete values of some continuous 'coefficient functions' (e.g. $a_j(t) = a(\mathbf{x}_j, t)$), the linear combinations in (5.1) may be rewritten using discrete convolution products in space, e.g.

$$\phi(\mathbf{x}, t) = \sum_{j=-\infty}^{\infty} a(\mathbf{x}_j, t) N^{(m)}(\mathbf{x} - \mathbf{x}_j) = \frac{(a_j(t) * N^{(m)})(\mathbf{x})}{\Delta x \Delta y} \tag{5.3}$$

where the two-dimensional discrete convolution product operator '$*$' is defined in Appendix A. The two-dimensional discrete Fourier transform is now found for the discrete convolution product as

$$\hat{\phi}(u, v; t) = \frac{\hat{a}(u, v; t)\hat{N}^{(m)}(u, v)}{\Delta x \Delta y} \tag{5.4}$$

Alternatively, the discrete Fourier transform of a coefficient function can be written as

$$\hat{a} = \Delta x \Delta y \frac{\hat{\phi}}{\hat{N}^{(m)}} \tag{5.5}$$

Similar calculations may of course be carried out for ϕ_z, η and their respective coefficient functions. Since spatial derivatives can be found by differentiating the basis functions like

$$\phi_x(\mathbf{x}, t) = \sum_{j=-\infty}^{\infty} a(\mathbf{x}_j, t) N_x^{(m)}(\mathbf{x} - \mathbf{x}_j) = \frac{(a(t) * N_x^{(m)})(\mathbf{x})}{\Delta x \Delta y} \tag{5.6}$$

the discrete Fourier transform of spatial derivatives can be found as

$$\hat{\phi}_x = \frac{\hat{a}\hat{N}_x^{(m)}}{\Delta x \Delta y} = \frac{\hat{N}_x^{(m)}}{\hat{N}^{(m)}}\hat{\phi} \tag{5.7}$$

It should be noted that only B-splines of order $m \geq 3$ have continuous first derivatives, as can be seen in Figure 2. This means that the analysis carried out here should apply to $m \geq 3$ only.

5.1. The boundary integral equation

The boundary integral equation (2.8) is considered for the field point and the source point both on the linearized free surface ($z = 0$). For the chosen discretization using B-splines, the first integral in (2.8) may after some manipulations be expressed as

$$I_1 = \int\int_{-\infty}^{\infty} \left[\sum_{j=-\infty}^{\infty} b_j(t) B_j^{(m)}(\xi) G(\mathbf{x} - \xi) \right] \mathrm{d}\xi = \frac{b * (N^{(m)} \otimes G)}{\Delta x \Delta y} \tag{5.8a}$$

Similarly, the second integral in (2.8) can be brought to the form

$$I_2 \equiv \int\int_{-\infty}^{\infty} \left[\sum_{j=-\infty}^{\infty} a_j(t) B_j^{(m)}(\xi) G_n(\mathbf{x} - \xi) \right] \mathrm{d}\xi = \frac{a * (N^{(m)} \otimes G_n)}{\Delta x \Delta y} \tag{5.8b}$$

Thus, the discrete Fourier transform in space of the discretized boundary integral equation can be written as

$$2\pi\hat{\phi} = \hat{\mathscr{F}}[I_1 - I_2] = \frac{\hat{b}\hat{\mathscr{F}}[N^{(m)} \otimes G]}{\Delta x \Delta y} - \frac{\hat{a}\hat{\mathscr{F}}[N^{(m)} \otimes G_n]}{\Delta x \Delta y} \tag{5.9}$$

This is rewritten introducing the discrete Fourier transforms of the coefficient functions, such as (5.4)

$$\frac{1 + \hat{S}_2}{\Delta x \hat{S}_1} \hat{\phi}(u, v; t) = \hat{\phi}_n(u, v; t) \tag{5.10}$$

with

$$\hat{S}_1 \equiv \frac{1}{2\pi \Delta x} \frac{\hat{\mathscr{F}}[N^{(m)} \otimes G]}{\hat{N}^{(m)}} \tag{5.11a}$$

$$\hat{S}_2 \equiv \frac{1}{2\pi} \frac{\hat{\mathscr{F}}[N^{(m)} \otimes G_n]}{\hat{N}^{(m)}} \tag{5.11b}$$

Using the continuous Fourier transforms of G, G_n (4.8) and $N^{(m)}$ (3.3) as well as the aliasing theorem (A.8), $\hat{S}_1$ and $\hat{S}_2$ are rewritten as

$$\hat{S}_1(\hat{u},\hat{v}) = \frac{\displaystyle\sum_{k=-\infty}^{\infty}\sum_{l=-\infty}^{\infty} \frac{(-1)^{m(k+l)}\left\{1+\exp\left(-4\pi\frac{h}{\Delta x}[(\hat{u}+k)^2+\alpha^2(\hat{v}+l)^2]^{1/2}\right)\right\}}{(\hat{u}+k)^m(\hat{v}+l)^m[(\hat{u}+k)^2+\alpha^2(\hat{v}+l)^2]^{1/2}}}{2\pi\displaystyle\sum_{k=-\infty}^{\infty}\sum_{l=-\infty}^{\infty}\frac{(-1)^{m(k+l)}}{(\hat{u}+k)^m(\hat{v}+l)^m}} \tag{5.12a}$$

$$\hat{S}_2(\hat{u},\hat{v}) = \frac{-\displaystyle\sum_{k=-\infty}^{\infty}\sum_{l=-\infty}^{\infty}\frac{(-1)^{m(k+l)}}{(\hat{u}+k)^m(\hat{v}+l)^m}\exp\left(-4\pi\frac{h}{\Delta x}[(\hat{u}+k)^2+\alpha^2(\hat{v}+l)^2]^{1/2}\right)}{\displaystyle\sum_{k=-\infty}^{\infty}\sum_{l=-\infty}^{\infty}\frac{(-1)^{m(k+l)}}{(\hat{u}+k)^m(\hat{v}+l)^m}} \tag{5.12b}$$

where $\alpha = \Delta x/\Delta y$ is the panel aspect ratio, and the summation index k should not be confused with the wavenumber κ. The relative wavenumber $(\hat{u}, \hat{v})$ is defined in Appendix A. It is obvious that even though $\hat{S}_1$ and $\hat{S}_2$ are given as functions only of the relative wave number $(\hat{u}, \hat{v})$, the terms depend also on the order m of the B-spline basis, the panel aspect ratio α and the relative water depth $h/\Delta x$. For quadratic basis functions ($m = 3$) and deep water ($\Delta x/h = 0$); this result was also obtained by Kring [11] and Vada [15].

5.2. Free surface conditions

The linearized kinematic and dynamic free-surface boundary conditions (2.6) and (2.7) are discretized using linear combinations of the basis functions (5.1) for the main variables. When expressions like (5.7) are used for spatial derivatives of the basis functions, the discrete Fourier transform in space yields

$$\frac{\partial\hat{\eta}}{\partial t} = -\left[U\frac{\hat{N}_x^{(m)}}{\hat{N}^{(m)}} + V\frac{\hat{N}_y^{(m)}}{\hat{N}^{(m)}}\right]\hat{\eta} + \hat{\phi}_n \tag{5.13}$$

$$\frac{\partial\hat{\phi}}{\partial t} = -\left[U\frac{\hat{N}_x^{(m)}}{\hat{N}^{(m)}} + V\frac{\hat{N}_y^{(m)}}{\hat{N}^{(m)}}\right]\hat{\phi} + g\hat{\eta} \tag{5.14}$$

Introducing $\hat{D}(u) = \mathrm{i}\Delta x\hat{N}_x^{(m)}/\hat{N}^{(m)}$ gives

$$\frac{\partial\hat{\eta}}{\partial t} = \mathrm{i}\left[U\frac{\hat{D}(u)}{\Delta x} + V\frac{\hat{D}(v)}{\Delta y}\right]\hat{\eta} + \hat{\phi}_n \tag{5.15}$$

$$\frac{\partial\hat{\phi}}{\partial t} = \mathrm{i}\left[U\frac{\hat{D}(u)}{\Delta x} + V\frac{\hat{D}(v)}{\Delta y}\right]\hat{\phi} - g\hat{\eta} \tag{5.16}$$

where $\hat{D}$ can be calculated as

$$\hat{D}(\hat{u}) = \frac{2\pi \sum_{k=-\infty}^{\infty} \dfrac{(-1)^{mk}}{(\hat{u}+k)^{m-1}}}{\sum_{k=-\infty}^{\infty} \dfrac{(-1)^{mk}}{(\hat{u}+k)^{m}}} \tag{5.17}$$

which for $m = 3$ corresponds to the results obtained by Kring [11] and Vada [15].

Time integration of the free-surface conditions '$\partial y/\partial t = f(t)$' is often performed using linear multi-step methods (K-step formulae) of the form

$$\sum_{j=0}^{K} \alpha_j y^{n-K+j} = \Delta t \sum_{j=0}^{K} \beta_j f^{n-K+j} \tag{5.18}$$

where y is the quantity to be integrated in time, and f represents the remaining terms in the free-surface condition. This form includes well-known schemes like the Euler schemes, the Adams–Bashforth and the Adams–Moulton schemes as well as the backward difference formula (BDF) schemes. If $\beta_K = 0$, the scheme is explicit (a predictor method), and if $\beta_K \neq 0$, the scheme is implicit (a corrector method) and a solution is then often found through an iteration process. Connected to a linear multi-step method are the two characteristic polynomials

$$\psi(z) = \sum_{j=0}^{K} \alpha_j z^j, \qquad \chi(z) = \sum_{j=0}^{K} \beta_j z^j \tag{5.19}$$

A linear multi-step formula (5.18) can be considered as a discrete convolution product in time (see Appendix A), and thus it can be shown that the z transform of a K-step formula sum is (see, e.g. Vada [15])

$$\underset{\wedge}{\mathscr{F}}\left[\sum_{j=0}^{K} \alpha_j y^{n-K+j}\right] = z^{-K}\left[\sum_{j=0}^{K} \alpha_j z^j\right] \underset{\wedge}{y} \tag{5.20}$$

Here a sub-wedge denotes a z transform. When linear multi-step methods are used to time integrate the linearized free-surface boundary conditions, the z transform of (5.15) and (5.16) can be found as

$$\frac{\psi_1(z)}{\Delta t} \underset{\wedge}{\hat{\eta}} = \mathrm{i}\left[U\frac{\hat{D}(u)}{\Delta x} + V\frac{\hat{D}(v)}{\Delta y}\right]\chi_1(z) \underset{\wedge}{\hat{\eta}} + \chi_1(z)\underset{\wedge}{\hat{\phi}_n} \tag{5.21}$$

$$\frac{\psi_2(z)}{\Delta t} \underset{\wedge}{\hat{\phi}} = \mathrm{i}\left[U\frac{\hat{D}(u)}{\Delta x} + V\frac{\hat{D}(v)}{\Delta y}\right]\chi_2(z)\underset{\wedge}{\hat{\phi}} - g\chi_2(z) \underset{\wedge}{\hat{\eta}} \tag{5.22}$$

where the subscripts on ψ and χ indicate that two different multi-step methods may be employed, one for each free-surface condition. When multi-step schemes are chosen for a particular BEM, it should be noted that the implicit methods often have better stability behaviour than similar explicit methods. However, due to the fact that ϕ_n in the kinematic condition is obtained through the boundary integral equations, which often are rather expensive to solve, an explicit scheme

can then be chosen for this condition. In order to improve the overall stability, an implicit scheme can be chosen to time integrate the dynamic condition. Such combinations of implicit and explicit schemes have been used by, for example, Büchmann *et al.* [4] and Kim *et al.* [5].

5.3. The fully discretized dispersion relation

Combining the free-surface conditions (5.21) and (5.22) with the z transform of (5.10) yields

$$\left\{ g\frac{1+\hat{S}_2(\hat{u},\hat{v})}{\Delta x\hat{S}_1(\hat{u},\hat{v})} - \left(U\frac{\hat{D}(\hat{u})}{\Delta x}+V\frac{\hat{D}(\hat{v})}{\Delta y}\right)^2 + \left(U\frac{\hat{D}(\hat{u})}{\Delta x}+V\frac{\hat{D}(\hat{v})}{\Delta y}\right)\frac{-\mathrm{i}}{\Delta t}\left(\frac{\psi_1(z)}{\chi_1(z)}+\frac{\psi_2(z)}{\chi_2(z)}\right) + \frac{1}{(\Delta t)^2}\frac{\psi_1(z)\psi_2(z)}{\chi_1(z)\chi_2(z)}\right\}\hat{\hat{\phi}} = 0 \tag{5.23}$$

from which the discrete dispersion relation is obtained as

$$g\frac{1+\hat{S}_2(\hat{u},\hat{v})}{\Delta x\hat{S}_1(\hat{u},\hat{v})} - \left(U\frac{\hat{D}(\hat{u})}{\Delta x}+V\frac{\hat{D}(\hat{v})}{\Delta y}\right)^2 + \left(U\frac{\hat{D}(\hat{u})}{\Delta x}+V\frac{\hat{D}(\hat{v})}{\Delta y}\right)\frac{-\mathrm{i}}{\Delta t}\left(\frac{\psi_1(z)}{\chi_1(z)}+\frac{\psi_2(z)}{\chi_2(z)}\right) + \frac{1}{(\Delta t)^2}\frac{\psi_1(z)\psi_2(z)}{\chi_1(z)\chi_2(z)} = 0 \tag{5.24}$$

Each term in this discrete dispersion relation corresponds to the discretization of a term in the continuous dispersion relation (4.9). For example, $(1+\hat{S}_2)/(\Delta x\hat{S}_1)$ is an approximation of $\kappa\tanh\kappa h$, and $\psi_1\psi_2/(\Delta t^2\chi_1\chi_2)$ is an approximation of $-\omega^2$. Alternatively, the discrete dispersion relation can be written in a non-dimensional form as

$$\hat{W}(z) = 0 \tag{5.25}$$

with

$$\hat{W}(z) = \left[\frac{1+\hat{S}_2(\hat{u},\hat{v})}{\hat{S}_1(\hat{u},\hat{v})} - F_h^2(\hat{D}(\hat{u})+\gamma\alpha\hat{D}(\hat{v}))^2\right]\chi_1(z)\chi_2(z) + \beta^2\psi_1(z)\psi_2(z) - \mathrm{i}F_h\beta(\hat{D}(\hat{u})+\gamma\alpha\hat{D}(\hat{v}))(\psi_1(z)\chi_2(z)+\psi_2(z)\chi_1(z)) \tag{5.26}$$

where the following dimensionless variables have been introduced:

$$F_h = \frac{U}{\sqrt{g\Delta x}}, \qquad \beta = \frac{\sqrt{\Delta x/g}}{\Delta t}, \qquad \alpha = \frac{\Delta x}{\Delta y}, \qquad \gamma = \frac{V}{U} \tag{5.27}$$

F_h is the grid Froude number, β is the grid number and α is the panel aspect ratio as previously defined. Without loss of generality it may be assumed that the 'current heading parameter' γ has a finite value. The dimensional form of the dispersion relation (5.24) is preferred for comparisons with the continuous dispersion relation (in calculations of convergence rates), while the non-dimensional form (5.25) is convenient when determining stability properties.

6. ACCURACY OF THE BEM

In order to determine the accuracy of the time-domain BEM, the discrete dispersion relation (5.24) should be compared with its continuous counterpart (4.9). The comparison of the two dispersion relations is straightforward when first rewriting the continuous dispersion relation (4.9) as

$$g\kappa \tanh \kappa h - (Uu + Vv)^2 + (Uu + Vv)2\omega - \omega^2 = 0 \tag{6.1}$$

and then comparing (5.24) and (6.1) term by term. The correspondence of the various terms in (5.24) and (6.1) can (for fixed α) be written as

$$\frac{-\mathrm{i}}{\Delta t}\left(\frac{\psi_1(z)}{\chi_1(z)} + \frac{\psi_2(z)}{\chi_2(z)}\right) = 2\omega[1 + O(\Delta t^{n_1})] \tag{6.2a}$$

$$\frac{1}{(\Delta t)^2}\frac{\psi_1(z)\psi_2(z)}{\chi_1(z)\chi_2(z)} = -\omega^2[1 + O(\Delta t^{n_2})] \tag{6.2b}$$

$$\frac{\hat{D}(\hat{u})}{\Delta x} = u[1 + O(\Delta x^{n_d})], \qquad \frac{\hat{D}(\hat{v})}{\Delta y} = v[1 + O(\Delta x^{n_d})] \tag{6.2c}$$

$$\frac{1 + \hat{S}_2(\hat{u}, \hat{v})}{\Delta x \hat{S}_1(\hat{u}, \hat{v})} = \kappa \tanh(\kappa h)[1 + O(\Delta x^{n_s})] \tag{6.2d}$$

where n_1 and n_2 depend on the choice of time integration scheme and give the temporal convergence rate, while n_d and n_s depend on the order of the B-spline basis and give the spatial convergence rate. In the following sections, the temporal convergence rates n_1 and n_2 and the spatial convergence rates n_d and n_s will be found by using a Taylor expansion approach in time or space for each of the above terms.

6.1. Temporal convergence rate

In general, the temporal convergence rate of the discrete dispersion relation can be found as $\min(n_1, n_2)$. The right-hand sides of (6.2a) and (6.2b) can be Taylor-expanded in time about $\omega \equiv \omega\Delta t = 0$ to find the order of the error terms. However, for more complicated multi-step schemes this procedure is rather laborious, and therefore the convergence behaviour of the rational expressions $(\psi_1/\chi_1) + (\psi_2/\chi_2)$ and $\psi_1\psi_2/\chi_1\chi_2$ are studied numerically.

It is straightforward to examine numerically the convergence rate of a function to a limit known *a priori*. In this particular case, the error terms in (6.2a) and (6.2b) are isolated and plotted on a log-scale as a function of $\hat{\omega}$. When a particular scheme is examined, the $\min(n_1, n_2)$ is important for the temporal convergence. Thus, it may be appropriate to examine the (relative) error on each scheme using a definition as

$$|\mathrm{E}| = \left| \frac{\mathrm{i}}{2\hat{\omega}} \left(\frac{\psi_1(z)}{\chi_1(z)} + \frac{\psi_2(z)}{\chi_2(z)} \right) + 1 \right| + \left| \frac{1}{\hat{\omega}^2} \frac{\psi_1(z)\psi_2(z)}{\chi_1(z)\chi_2(z)} + 1 \right| = O(\hat{\omega}^{n_1}) + O(\hat{\omega}^{n_2}) = O(\hat{\omega}^{\min(n_1,n_2)}) \tag{6.3}$$

with $z = \exp \mathrm{i}\omega\Delta t = \exp \mathrm{i}\hat{\omega}$. It should be noted that $|\mathrm{E}|$ does not yield the actual error on a particular scheme only the overall convergence behaviour.

The explicit Euler scheme has the characteristic polynomials

$$\psi(z) = z - 1, \qquad \chi(z) = 1 \tag{6.4}$$

while for the implicit Euler scheme, the polynomials read

$$\psi(z) = z - 1, \qquad \chi(z) = z \tag{6.5}$$

Analytical Taylor expansions in time show that the fully explicit and the fully implicit Euler schemes both are of the order $n_1 = n_2 = 1$, each with $|\mathrm{E}| = 3\hat{\omega}/2 + \cdots$, while the mixed implicit–explicit Euler scheme is of the order $n_1 = n_2 = 2$ with $|\mathrm{E}| = \hat{\omega}/4 + \cdots$. These results are confirmed by plotting the numerically found values of $|\mathrm{E}|$ as a function of $\hat{\omega}$ for each of the three schemes (Figure 4). It is noted from the figure that the mixed Euler scheme is indeed one order more accurate than each of the two pure Euler schemes. As a comparison, the rapid temporal convergence of a mixed fourth-order implicit–explicit Adams (AM4–AB4) scheme is also shown on the figure.

6.2. Spatial convergence rate

The spatial convergence rate of the time-domain BEM depends on the terms $\hat{D}$ and $(1 + \hat{S}_2)/\hat{S}_1$ in (6.2). The convergence behaviour of each of these terms will be studied in the following to obtain results for n_d and n_s.

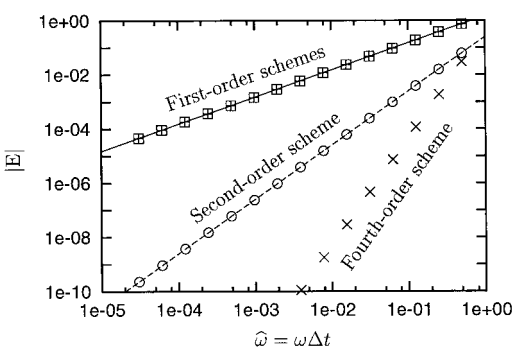

Figure 4. Error terms for the explicit (+), implicit (□), and mixed (○) Euler schemes, and for the mixed implicit–explicit fourth-order Adams scheme (×). Shown are also the functions $3\hat{\omega}/2$ (—) and $\hat{\omega}^2/4$ (---).

It is obvious from (5.17) that both the numerator and the denominator of $\hat{D}$ have a singularity at $\hat{u}=0$. Thus, it is convenient for $\hat{u}\neq 0$ to rewrite (5.17) as

$$\hat{D}(\hat{u}) = 2\pi\hat{u}\,\frac{\hat{D}_1}{\hat{D}_2} \tag{6.6}$$

with

$$\hat{D}_1 = \hat{u}^{m-1}\sum_{k=-\infty}^{\infty}\frac{(-1)^{mk}}{(\hat{u}+k)^{m-1}}, \qquad \hat{D}_2(\hat{u}) = \hat{u}^m\sum_{k=-\infty}^{\infty}\frac{(-1)^{mk}}{(\hat{u}+k)^m} \tag{6.7}$$

Then the convergence behaviour of the numerator and the denominator in (6.6) can be examined for $\hat{u}\to 0$. Following Nakos [12], the 'singular parts' (corresponding to the zero value of the summation index k) of $\hat{D}_1(\hat{u})$ and $\hat{D}_2(\hat{u})$ can be extracted, and the remaining terms can be Taylor-expanded around $\hat{u}=0$ to yield

$$\hat{D}_1(\hat{u}) = 1+\hat{u}^{m-1}\sum_{k\neq 0}\frac{(-1)^{mk}}{k^{m-1}}\left[1-\frac{m-1}{k}\,\hat{u}+O(\hat{u}^2)\right] \tag{6.8a}$$

$$\hat{D}_2(\hat{u}) = 1+\hat{u}^{m}\sum_{k\neq 0}\frac{(-1)^{mk}}{k^{m}}\left[1-\frac{m}{k}\,\hat{u}+O(\hat{u}^2)\right] \tag{6.8b}$$

The series above are absolutely convergent only for $m\geq 3$. Note that, due to symmetry, the first term in the square brackets of (6.8a) vanishes for even m. Similarly, the first term in the square bracket of (6.8b) vanishes for odd m, but this has no significance since in this case $\hat{D}_1$ limits the accuracy. It follows that for a fixed value of u

$$\frac{\hat{D}(\hat{u})}{\Delta x} = u\,\frac{\hat{D}_1(\hat{u})}{\hat{D}_2(\hat{u})} = \begin{cases} u[1+O(\Delta x^{m-1})], & m \text{ odd} \\ u[1+O(\Delta x^{m})], & m \text{ even} \end{cases} \tag{6.9}$$

and thus

$$n_d = \begin{cases} m-1, & m \text{ odd} \\ m, & m \text{ even} \end{cases}, \qquad m\geq 3 \tag{6.10}$$

The process to find the spatial convergence rate of $(1+\hat{S}_2)/\hat{S}_1$ is similar, albeit more laborious. In this case, Taylor expansion in two dimensions $(\hat{u},\hat{v})$ is needed, and the expressions get more complicated. First the fraction in (5.10) is rewritten as

$$\frac{1+\hat{S}_2(\hat{u},\hat{v})}{\Delta x\hat{S}_1(\hat{u},\hat{v})} = 2\pi\,\frac{F_1(\hat{u},\hat{v})-F_2(\hat{u},\hat{v})}{F_3(\hat{u},\hat{v})} \tag{6.11}$$

where the functions

$$F_1(\hat{u}, \hat{v}) = \hat{u}^m \hat{v}^m \sum_{k=-\infty}^{\infty} \sum_{l=-\infty}^{\infty} \frac{(-1)^{m(k+l)}}{(\hat{u}+k)^m(\hat{v}+l)^m} \tag{6.12a}$$

$$F_2(\hat{u}, \hat{v}) = \hat{u}^m \hat{v}^m \sum_{k=-\infty}^{\infty} \sum_{l=-\infty}^{\infty} \frac{(-1)^{m(k+l)}}{(\hat{u}+k)^m(\hat{v}+l)^m} \exp\left(-4\pi \frac{h}{\Delta x} [(\hat{u}+k)^2 + \alpha^2(\hat{v}+l)^2]^{1/2} \right) \tag{6.12b}$$

$$F_3(\hat{u}, \hat{v}) = \Delta x \hat{u}^m \hat{v}^m \sum_{k=-\infty}^{\infty} \sum_{l=-\infty}^{\infty} \frac{(-1)^{m(k+l)} \left\{ 1 + \exp\left(-4\pi \frac{h}{\Delta x} [(\hat{u}+k)^2 + \alpha^2(\hat{v}+l)^2]^{1/2} \right) \right\}}{(\hat{u}+k)^m(\hat{v}+l)^m [(\hat{u}+k)^2 + \alpha^2(\hat{v}+l)^2]^{1/2}} \tag{6.12c}$$

have been introduced for convenience. In the asymptotic expansions for each of the above functions, the double summations are divided into four distinct parts corresponding to relative importance. The main part corresponds to the zero value of both summation indices, i.e. $k = l = 0$. The leading 'error terms' corresponds to $k = 0$ with $l \neq 0$ and to $l = 0$ with $k \neq 0$. The remaining terms, where both summation indices are non-zero, are higher-order terms in the asymptotic expansion. Thus, for example, F_1 is rewritten as

$$F_1(\hat{u}, \hat{v}) = 1 + \hat{u}^m \sum_{k \neq 0} \frac{(-1)^{mk}}{(\hat{u}+k)^m} + \hat{v}^m \sum_{l \neq 0} \frac{(-1)^{ml}}{(\hat{v}+l)^m} + \hat{u}^m \hat{v}^m \sum_{k \neq 0} \sum_{l \neq 0} \frac{(-1)^{m(k+l)}}{(\hat{u}+k)^m(\hat{v}+l)^m} \tag{6.13}$$

The leading 'error terms' are then Taylor-expanded to find the asymptotic behaviour for small $\hat{u}$, $\hat{v}$. Finally, the functions can, for fixed (u, v), be written as

$$F_1(\hat{u}, \hat{v}) = \begin{cases} 1 + O(\Delta x^{m+1}), & m \text{ odd} \\ 1 + O(\Delta x^m) & m \text{ even} \end{cases} \tag{6.14a}$$

$$F_2(\hat{u}, \hat{v}) = \exp(-2h\sqrt{u^2+v^2}) \left[1 + \exp\left(\frac{\Delta x}{h} \right) O(\Delta x^m) \right] \tag{6.14b}$$

$$F_3(\hat{u}, \hat{v}) = \begin{cases} (2\pi/\sqrt{u^2+v^2})\{1 + \exp(-2h\sqrt{u^2+v^2})\}[1 + O(\Delta x^{m+2})], & m \text{ odd} \\ (2\pi/\sqrt{u^2+v^2})\{1 + \exp(-2h\sqrt{u^2+v^2})\}[1 + O(\Delta x^{m+1})], & m \text{ even} \end{cases} \tag{6.14c}$$

It should be noted that F_2 has an exponential convergence behaviour, so it is F_1 that limits the convergence of $(1 + \hat{S}_2)/\hat{S}_1$. Combining (6.11) and (6.14) yields

$$\frac{1 + \hat{S}_2(\hat{u}, \hat{v})}{\Delta x \hat{S}_1(\hat{u}, \hat{v})} = \begin{cases} \kappa \tanh(\kappa h)[1 + O(\Delta x^{m+1})], & m \text{ odd} \\ \kappa \tanh(\kappa h)[1 + O(\Delta x^m)], & m \text{ even} \end{cases} \tag{6.15}$$

where $\kappa = \sqrt{u^2+v^2}$ is not to be confused with the summation index k. Thus

$$n_s = \begin{cases} m+1, & m \text{ odd} \\ m, & m \text{ even} \end{cases}, \quad m \geq 3 \tag{6.16}$$

The spatial convergence rates (6.10) and (6.16) can be verified numerically in the same manner as the temporal convergence rates, i.e. by plotting the relative error terms against grid size on a logarithmic scale. Expressions for the relative error terms are easily found by isolating the order functions in (6.2). The relative error as a function of the mesh size is depicted in Figure 5 for one particular choice of panel aspect ratio, relative water depth, and angle of incidence of the waves. The error terms have been found numerically for a number of the terms as discussed above and the analytical convergence rates (6.10), (6.16) are confirmed. Even though results are only given for orders three and four and for one particular case in this work, calculations have also been carried out for the basis function of orders five through to nine, as well as for different wave angles, water depths, and panel aspect ratios, and in these cases the analytical results have been confirmed too.

In general, the spatial convergence rate of the discrete dispersion relation (5.24) is given by $\min(n_d, n_s)$. Since, for all values of m, $n_d \leq n_s$ it is n_d that in general limits the spatial convergence rate. However, in a zero current situation the terms connected with n_d vanish, and thus n_s yields the spatial convergence rate.

7. STABILITY OF THE DISCRETE DISPERSION RELATION

It is noted from (5.25) that the discrete dispersion relation can be written as a polynomial in $z = \exp \mathrm{i}\omega\Delta t$. Thus, solving the discrete dispersion relation corresponds to finding the roots of a complex polynomial in z. This can be done, for example, by finding the eigenvalues of the companion matrix (see, e.g. Press *et al.* [23]). Numerically, the solution of the discrete dispersion relation degenerates into solving an eigenvalue problem for a matrix, which can be done by any well-documented linear algebra package, such as LAPACK [24]. Alternatively, for low-order schemes, the roots of the polynomial can be found analytically.

For a fixed wavenumber vector $(\hat{u}, \hat{v})$, each of the roots of $\hat{W}(z)$ corresponds to a solution where the temporal behaviour depends on the value of the root

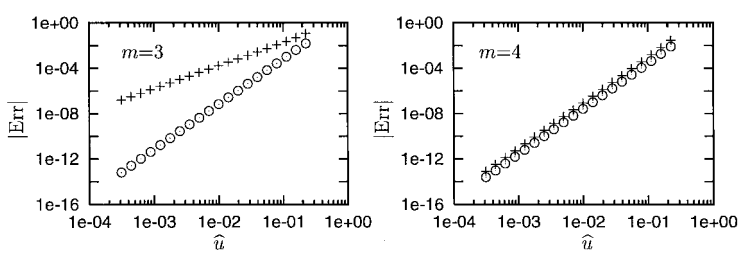

Figure 5. Examples of error terms for the spatial convergence of $\hat{D}/\Delta x$ (+), see (6.9), and $(1 + \hat{S}_2)/(\Delta x \hat{S}_1)$ (○), see (6.15), for fixed panel aspect ratio, $\alpha = 1$, relative water depth, $h\sqrt{u^2 + v^2} = \kappa h = 1$, and a wave direction given by $u/v = 2$. The errors are normalized by the analytically found limits and are given for two different orders of the basis functions ($m = 3, 4$).

$$z_j = |z_j| \exp \mathrm{i}\omega_j \Delta t \tag{7.1}$$

Here $|z_j|$ and $\omega_j \Delta t$ represent respectively the modulus and argument of the complex number z_j. Any deviation of $|z_j|$ from unity represents damping ($|z_j| < 1$) or amplification ($|z_j| > 1$) of the solution in time. If for some $(\hat{u}, \hat{v})$ any of the roots have modulii greater than unity, then those particular solutions will grow unbounded in time, and the scheme is denoted 'unstable'. If for all $(\hat{u}, \hat{v})$ and for all choices of time step size all roots have modulii smaller than unity, then all the corresponding solutions will decrease in time, and the scheme is denoted 'strongly stable'. Only if the maximum value of the modulii of the eigenvalues is exactly unity, will there exist a solution that is periodic in time. A scheme with this property is denoted 'neutrally stable'. If the temporal and spatial discretization of the dispersion relation is 'good' (in some sense), then two of the roots of $\hat{W}(z)$ (5.25), called the 'main roots', should correspond closely to the two solutions of ω from the continuous dispersion relation (4.9). The remaining roots of $\hat{W}(z)$ (if any) are called spurious roots. Spurious roots will result in spurious (non-physical) waves in the numerical model. Thus, the modulii of all the spurious roots should be kept as small as possible in order to suppress the spurious solutions in the numerical model. On the other hand, the modulii of the two main roots should be close to unity to conserve energy on the two main frequencies. It should be noted that the Euler schemes discussed in the following have no spurious roots.

Vada and Nakos [14] examined the stability properties of several different time stepping schemes for use with their numerical model using a third-order B-spline basis and assuming deep water ($\Delta x/h = 0$) and a zero current angle with the grid ($V = 0$). Vada [15] gives more details with regard to how the actual stability diagrams are found, and shows also analytically some of the properties of the simpler schemes. It was shown that for their model the purely explicit Euler scheme is always unstable, while the purely implicit Euler scheme is strongly stable. Their conclusions are also valid for basis functions of higher order ($m \geq 3$), finite water depths and currents intersecting the model grid obliquely ($\gamma \neq 0$). The mixed implicit–explicit Euler scheme is neutrally stable if the time step size is small enough, i.e. if $\beta \geq \beta_c$, where the critical value of β depends on the grid Froude number, the panel aspect ratio, the water depth, and the current heading as

$$\beta_c(\alpha, F_h, \gamma, \Delta x/h) = \max_{\hat{u},\hat{v}} \left\{ \frac{1}{2} \left| \frac{1 + \hat{S}_2(\hat{u}, \hat{v})}{\hat{S}_1(\hat{u}, \hat{v})} - F_h(\hat{D}(\hat{u}) + \gamma\alpha\hat{D}(\hat{v})) \right| \sqrt{\frac{\hat{S}_1(\hat{u}, \hat{v})}{1 + \hat{S}_2(\hat{u}, \hat{v})}} \right\} \tag{7.2}$$

If $\beta < \beta_c$, then an instability will occur for at least one particular wavenumber, and this will of course make the scheme unstable. Even though the stability criterion for the mixed Euler scheme can be written on the form (7.2), numerical evaluations of $\hat{D}$, $\hat{S}_1$ and $\hat{S}_2$ are needed in order to obtain a value of β_c. Thus, this represents a semi-analytical method for finding the stability region for the mixed Euler scheme.

The stability of the scheme can also be examined by numerically calculating the roots of the dispersion relation for a wide range of wave numbers $(\hat{u}, \hat{v})$. The maximum modulus of the eigenvalues (over all $\hat{u}$ and $\hat{v}$) is then determining the stability of a scheme for one particular choice of spatial discretization, water depth, current and time step size. Thus, keeping the other parameters fixed the stability can be found as a function of the time step size by plotting

$\max_{j,\hat{u},\hat{v}} |z_j|$ against β. As an example we consider the mixed Euler scheme in the deep water case without current and for $\alpha = 1$, i.e. $\Delta x = \Delta y$, and use cubic B-splines ($m = 4$) (Figure 6). It is noted from the figure that exactly at $\beta = \beta_c$ predicted by (7.2), the largest modulus of the roots drops to unity with machine precision accuracy. For $\beta > \beta_c$ both roots of the mixed Euler scheme have modulus one.

The stability properties of the mixed Euler scheme for a range of different grid Froude numbers are shown in the stability diagram in Figure 7. It is noted from the figure that for low grid Froude numbers β_c is fairly independent of both F_h and the order of the B-spline basis. For larger current strengths β_c increases and thus smaller time steps are needed to maintain a stable scheme. For quadratic B-spline basis functions ($m = 3$), it was noted by Vada [15] in the stability analysis of the mixed implicit–explicit Euler scheme that the stability at low grid Froude numbers, F_h, does not depend on the Froude number itself, and that the stability at high grid Froude numbers does not depend on the panel aspect ratio, α. These observations hold true also for higher orders of the basis functions. At small grid Froude numbers the unstable wave numbers are located close to the corners of the principal wave number domain, i.e. with both $\hat{u}$ and $\hat{v}$ close to ± 0.5. For increasing F_h a new kind of instability occurs at relative wave numbers somewhat smaller than 0.5 and primarily in the direction of the current. This second type of instability is responsible for the increase in β_c with F_h observed in Figure 7.

The effect of the panel aspect ratio on the stability is shown in Figure 8. It is noted from the figure that for small F_h an increasing aspect ratio results in a less stable scheme. This effect is primarily due to the scaling of the axis, since both β and F_h are scaled by Δx. Thus, in Figure 8, increasing α can be regarded purely as decreasing Δy, and thus decreasing the overall panel size. Then, it should not be surprising that this results in a less stable scheme, with instabilities occurring at high wave numbers. Note that for high grid Froude numbers the stability does not depend on the panel aspect ratio, α.

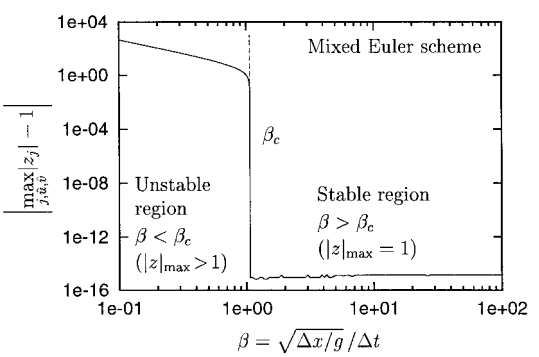

Figure 6. Maximum modulus of the roots of the mixed Euler schemes for varying β and fixed $\alpha = 1$, $F_h = 0$ and $m = 4$ in deep water. Results from numerical solution of the dispersion relation (—) and the (semi-analytical) critical value of β found by (7.2) is given (---).

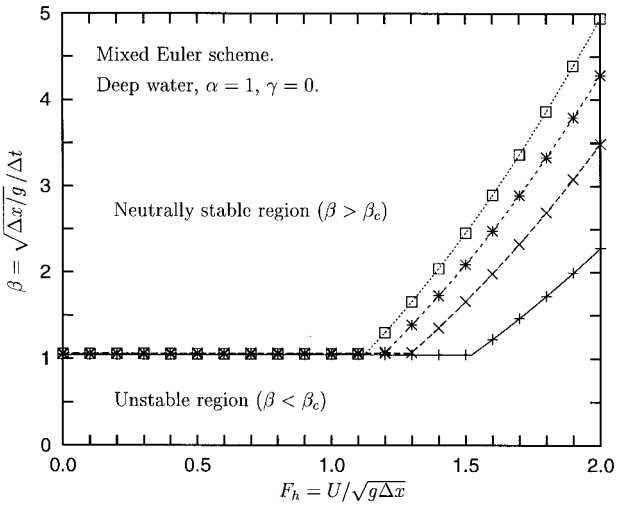

Figure 7. Stability diagram for the mixed implicit–explicit Euler scheme with $\alpha = 1$ and $\gamma = 0$ (corresponding to $V = 0$) in deep water. Results from numerical solution of the dispersion relation with B-spline basis functions of order $m = 3$ (+), 4 (×), 5 (- ∗ -), and 6 (□). Semi-analytical results using (7.2) for B-spline basis functions of order $m = 3$ (—), 4 (– – –), 5 (---) and 6 (· · ·).

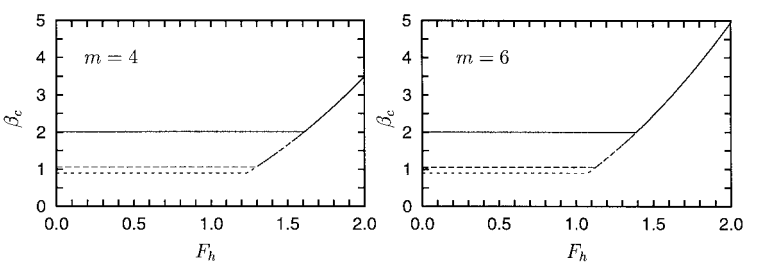

Figure 8. Panel aspect ratio effects on the stability of the mixed Euler scheme for two different orders of the B-spline basis ($m = 4$ and $m = 6$). Results are shown for three different aspect ratios: $\alpha = 5.0$ (—), $\alpha = 1.0$ (– – –), and $\alpha = 0.2$ (---). All cases are assuming deep water with current heading parameter $\gamma = 0$.

The effect of the water depth on the stability is very small except in very shallow water (say when $h/\Delta x < 1$) (see Figure 9). The physical interpretation of this result is based on the wavelengths on which the instabilities occur. Generally, the short waves (close to grid scale) are harder to resolve and, as mentioned above, for unstable schemes it is often these short waves that are exponentially growing in time. In general, these waves cannot 'feel the bottom', except for, say, $\kappa h < \pi$ (a typical deep water limit). For the short waves with wavelengths around $2\Delta x$,

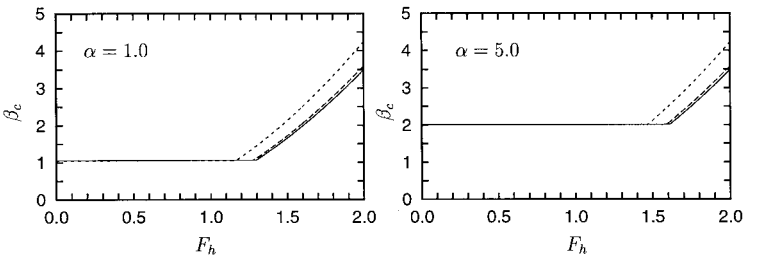

Figure 9. Water depth effects on the stability of the mixed Euler scheme. Results are shown for three different water depths: deep water (—), $h/\Delta x = 1.0$ (– – –), and $h/\Delta x = 0.5$ (---) and two different panel aspect ratios ($\alpha = 1$ and $\alpha = 5$). All cases use $\gamma = 0$ and $m = 4$.

the deep water limit obviously yields $h/\Delta x < 1$. It should be noted from Figure 9 that even in very shallow water (say, $h/\Delta x = 0.5$) only the stability at relatively large grid Froude numbers is affected by the finite water depth. For low grid Froude numbers there are virtually no stability effects from the finite water depth.

As can be seen from Figure 10, the current heading has a quite significant effect on the stability of the scheme. In Figure 10, the abscissae have been scaled such that they represent the (normalized) absolute values of the current rather than just the current in the x-direction. Even though the effects of the current heading are hard to quantify in detail, it is evident that turning the current to go 'along' the panels results in a more stable scheme. It is also noticed that for small grid Froude numbers the stability is not affected by the current heading or the absolute value of the current.

A stability diagram of the mixed implicit–explicit fourth-order Adams scheme is shown in Figure 11. The instabilities observed in the AM4–AB4 scheme correspond to spurious roots in the discrete dispersion relation. At zero speed, the instabilities appear primarily at $\hat{u}$ and $\hat{v}$ both close to ± 0.5, but even at low grid Froude numbers the wave numbers of the instabilities shift in the direction of the current away from the corners of the principal wave number regime. Also, as can be seen from Figure 11, the critical value of β increases with the current strength even for small F_h. As noticed by Vada and Nakos [14], the mixed implicit–explicit fourth-order Adams scheme has significant damping of the main roots when β is close to the stability limit. However, this property is not necessarily undesirable, since only the shorter waves are affected by this dissipation. For the longer waves, the modulii of the main roots are very close to unity.

The effect of the panel aspect ratio on the stability of the mixed fourth-order Adams scheme is shown in Figure 12 for one particular choice of basis functions, current heading and water depth. It is noted that increasing the panel aspect ratio results in a less stable scheme as in the case for the mixed Euler scheme. Also, the effect of the aspect ratio decreases with increasing current strength, as the panel length in the current direction becomes the more important parameter.

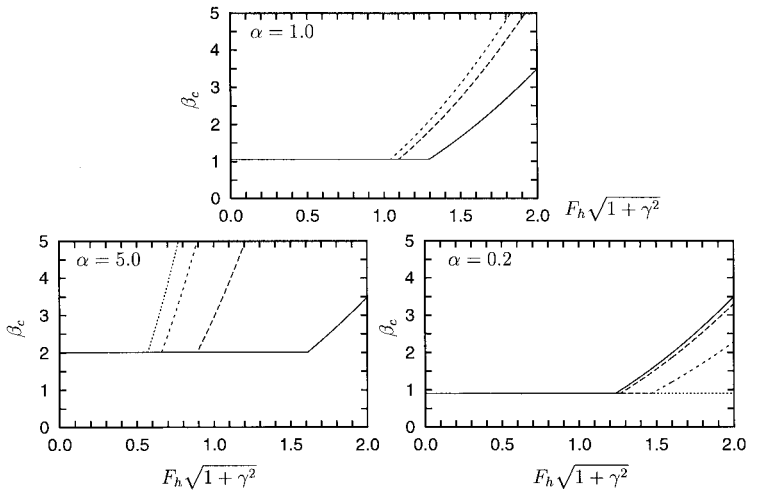

Figure 10. Effect of angle between current and panels on the stability of the mixed Euler scheme for $m = 4$ in deep water. Results are shown for four different current headings: $\gamma = 0.0$ (—), $\gamma = 0.5$ (– – –), $\gamma = 1.0$ (---) and $\gamma = 2.0$ ($\cdots$). For $\alpha = 1$ the curves for $\gamma = 0.5$ and $\gamma = 0.2$ are indistinguishable, and thus only the first is actually plotted. Note that the curves for $\alpha = 5.0$ with $\gamma = 0.5$, 1.0 and 2.0 each matches respectively the curves for $\alpha = 0.2$ with $\gamma = 2.0$, 1.0 and $\gamma = 0.5$ due to symmetry. The only difference on each of these pairs of curves is the scaling of the axes.

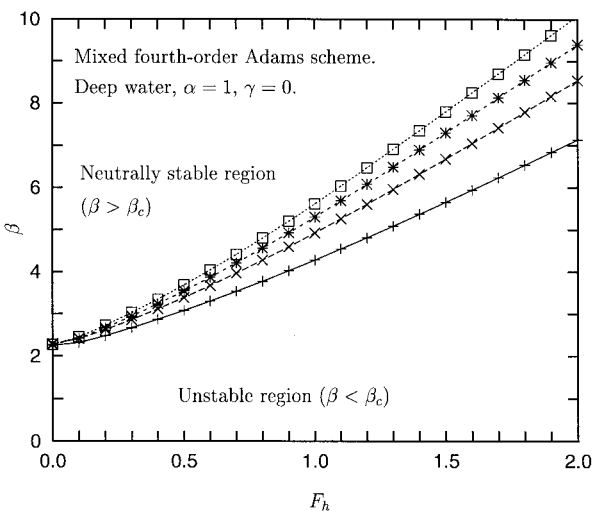

Figure 11. Stability diagram for the mixed implicit–explicit fourth-order Adams scheme with $\alpha = 1$ and $\gamma = 0$ (corresponding to $V = 0$) in deep water. Results from numerical solution of the dispersion relation with B-spline basis functions of order $m = 3$ (+), 4 (– × –), 5 (- ∗ -), and 6 ($\cdot\cdot\square\cdot\cdot$).

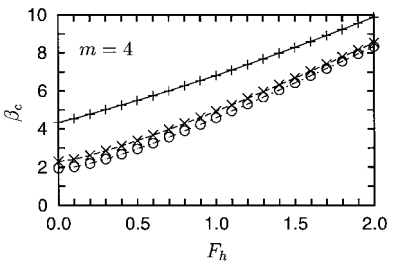

Figure 12. Effects of panel aspect ratio on the stability of the mixed fourth-order Adams scheme using a piecewise cubic B-spline basis ($m = 4$). Results are shown for three different aspect ratios: $\alpha = 5.0$ (+), $\alpha = 1.0$ (- × -) and $\alpha = 0.2$ (-○-). All cases are assuming deep water with $\gamma = 0$.

8. DISPERSION RELATION RESULTS AND EXAMPLES

As mentioned in the previous sections, the spatial convergence rate and the temporal convergence rate are fully separated parameters. Thus, no matter how small the time step is, there will be a finite error due to the spatial discretization. This error, of course, limits the accuracy that can be obtained with the chosen scheme and spatial discretization. Note that this limit is the same for all the multi-step time integration schemes considered. So, if the temporal convergence of a particular scheme is to be examined, then it should be kept in mind that, for example, the frequencies will converge to the limit yielded by the chosen spatial discretization rather than to the 'true' solution yielded by the continuous dispersion relation.

When the non-dimensional parameters (5.27) and (A.2) are introduced, the continuous dispersion relation (4.9) can be rewritten as

$$\beta\omega\Delta t = 2\pi F_h(\hat{u} + \alpha\gamma\hat{v}) \pm \sqrt{2\pi\sqrt{\hat{u}^2 + \alpha^2\hat{v}^2}\tanh\left[\frac{h}{\Delta x}\,2\pi\sqrt{\hat{u}^2 + \alpha^2\hat{v}^2}\right]} \tag{8.1}$$

As an example, consider the discrete dispersion relation with $\hat{v} = 0$ and $\alpha = 1$ in deep water. Figure 13A shows temporally converged results for $\beta\omega\Delta t$ for the discrete dispersion relation for different orders of the B-spline basis. Also shown is the continuous result. Note that only the upper branch of the dispersion relation is shown in the figure. It is noted that the discrete results and continuous results agree well for small $\hat{u}$—corresponding to longer waves. Examining the difference more closely (Figure 13B) it is noted that for moderate values of $\hat{u}$ the limiting error on the discrete dispersion relation is a strongly decreasing function of the order of the B-spline basis. Thus, for say $\hat{u} = 0.2$, the limiting error on $\beta\omega\Delta t$ decays rapidly for increasing m. For values of $\hat{u}$ close to the Nyquist frequency ($\hat{u} = \pm 0.5$) all the discrete schemes perform poorly, which is to be expected.

Introducing a current in a direction parallel to the panels the behaviour of the dispersion relation is changed significantly as can be seen from Figure 14. Again only the upper branch of the dispersion relation is shown. It is noted especially by comparing Figures 13B and 14B that the errors on the discrete dispersion relation increase dramatically with the introduction

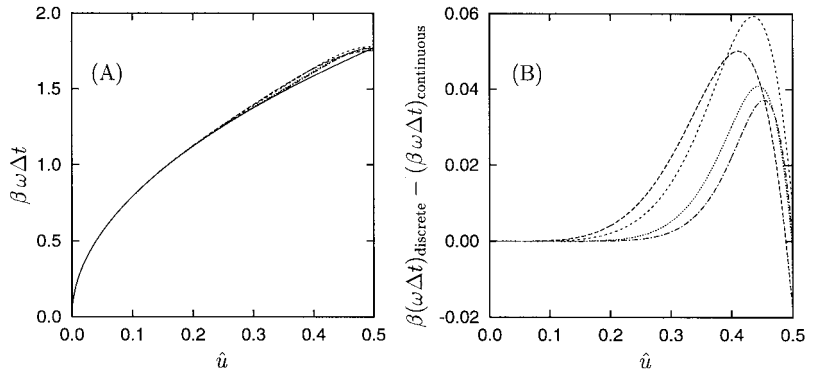

Figure 13. Limiting dispersion relations ($\beta \to \infty$) for all multi-step time integration schemes in deep water, without current and using ($\alpha = 1$) and ($\hat{v} = 0$). The plot (A) shows the continuous dispersion relation (—) and the limiting discrete dispersion relation for $m = 3$ (– – –), $m = 4$ (---), $m = 5$ (· · ·) and $m = 6$ (- · -). The plot (B) shows the errors on the discrete solutions compared to the continuous solution. In the actual computations the mixed Euler scheme with $\beta = 10^4$ has been used.

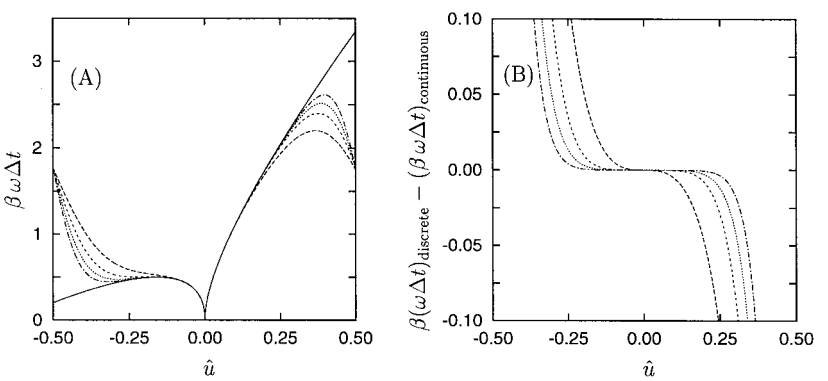

Figure 14. Limiting dispersion relations ($\beta \to \infty$) for all multi-step time integration schemes in deep water with current ($F_h = 0.5$), for $\alpha = 1$, $\gamma = 0$ and $\hat{v} = 0$. The plot (A) shows the continuous dispersion relation (—) and the limiting discrete dispersion relation for $m = 3$ (– – –), $m = 4$ (---), $m = 5$ (· · ·) and $m = 6$ (- · -). The plot (B) shows the errors on the discrete solutions compared with the continuous solution, i.e. $\beta(\omega\Delta t)_{\text{discrete}} - \beta(\omega\Delta t)_{\text{continuous}}$. In the actual computations the mixed Euler scheme with $\beta = 10^4$ has been used.

of a current. A part of this error is caused by the fact that the discrete dispersion relation is both continuous and periodic in $\hat{u}$ (and $\hat{v}$). Thus, for the discrete dispersion relation $\beta\omega\Delta t$ must have the same value at $\hat{u} = -0.5$ and $\hat{u} = 0.5$ (fixed $\hat{v}$). Since, in the continuous dispersion relation, $\beta\omega\Delta t$ differs considerably at these two values of $\hat{u}$, a significant error must

be expected on the discrete dispersion relation as $|\hat{u}| \to 0.5$, even for basis functions of very high order.

It should be noted that in the case of no current n_s (6.16) rather than n_d (6.10) limits the spatial convergence rates for $\hat{u} \to 0$. This gives as a result that the schemes based on B-splines of odd orders (e.g. $m = 3$) have better convergence properties for $F_h = 0$ than for $F_h \neq 0$. Obviously, this means that when a current is included, more nodes per wavelength will be required to obtain a particular accuracy if a scheme based on B-splines of an odd order is used. If high accuracy is needed (e.g. a relative error smaller than 0.1 per cent) the necessary number of nodes per wave length increases from 7 to 19 using third-order (quadratic) basis functions when the current increases from $F_h = 0$ to $F_h = 0.5$. Similarly, when fourth-order (cubic) B-splines are used, the number of nodes per wavelength needed for this accuracy increases only from around 6 to around 7. It should be noted that these conclusions are based on the data shown in Figures 13 and 14 and could change somewhat by the inclusion of, for example, a current under an oblique angle with the model grid. However, the numbers suggest that for most applications a fourth-order B-spline basis should be sufficient to obtain good accuracy with a modest number of unknowns.

For practical applications, the actual error on a particular scheme for a particular (finite) time step size is more interesting than the (limiting) convergence behaviour. Thus, the discrete dispersion relation should be examined for varying time step sizes in order to examine more closely the error on each particular scheme. For a chosen scheme and discretization in time and space (and a fixed current) the accuracy of the discrete dispersion relation can be found for all wavenumbers and contours for, e.g. the relative error on $\beta\omega\Delta t$ can be found. Examples of this application of the present analysis are shown in Figure 15. It is noted from the figure that when the time step size is fairly large (corresponding to $\beta = 4$ on the figure) the choice of the time stepping scheme has a great impact on the accuracy of the solution, but for smaller time step sizes (corresponding to $\beta = 16$ on the figure) both schemes are nearly converged in time, and the choice of scheme has little impact on the accuracy. Thus, if an 'optimum' scheme and time step size is sought for a specific problem, then both accuracy and stability constraints should be satisfied. Of course, in an actual application of a time-domain BEM it is not feasible to examine this in detail. Rather, a 'fairly stable' scheme (such as the mixed Euler scheme) should be chosen and then the time step size should be chosen sufficiently small to satisfy some 'worst case' conditions of stability and accuracy requirements.

9. CONCLUSIONS AND DISCUSSION

The accuracy and stability properties of a family of perturbation-based time-domain boundary element models (BEMs) with B-spline basis functions have been examined. It has been shown that the spatial convergence rate equals n_s in a no-current case and n_d when a current is present, where n_d and n_s are defined by respectively by (6.10) and (6.16). In general, the accuracy increases with increasing order of the B-spline basis functions.

Furthermore, BEMs based on odd basis functions have an advantage in no-current cases, but a disadvantage when a current is present. This behaviour seems in general to favour models based on B-splines of even order, especially if the order of the basis is hard-coded in

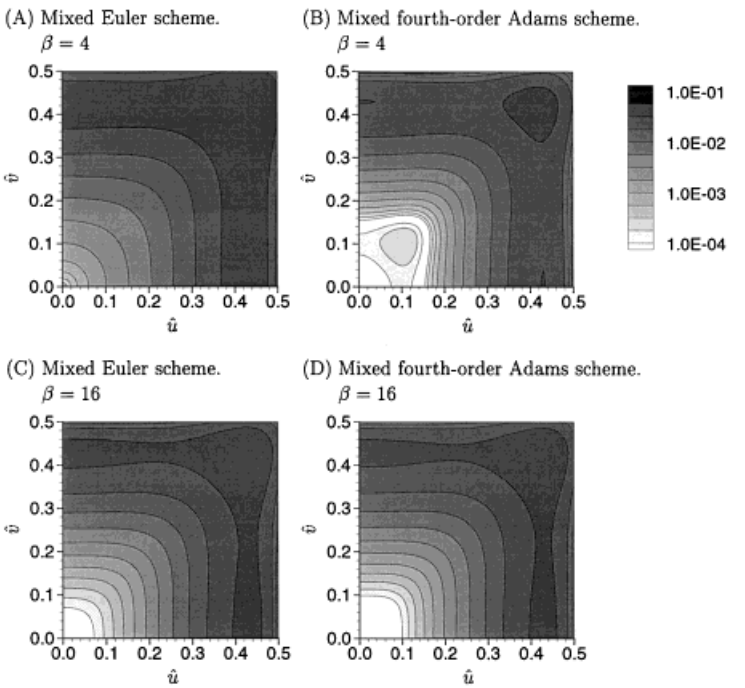

Figure 15. Relative error on the frequency ($\beta\omega\Delta t$) for the upper branch of the dispersion relation using two different time integration schemes and two different time step sizes. In all the calculations $m = 4$, $\alpha = 1$, $F_h = 0$ and deep water are used. Due to symmetry the error contours in the remaining three quadrants of the principal wave number regime can be found by reflecting the given plots around the $\hat{u}$ and $\hat{v}$ axis.

the BEM source code rather than controlled at runtime. In a particular example, the number of nodes per wavelength needed to obtain a specified accuracy increases from 7 to 19 by the introduction of a current when third-order B-splines basis functions are used. When fourth-order B-splines are used, the corresponding increase is only from around 6 to around 7 nodes per wavelength. For practical applications fourth-order B-splines (piecewise cubic polynomials) should be sufficient to obtain good accuracy with a modest number of unknowns. It should be noted that the conditioning of the linear system obtained in the BEM often becomes considerably worse with increasing order of the B-spline basis [10]. This phenomenon and methods to avoid the ill conditioning will be discussed in detail in future work. For the temporal convergence it has been shown that the mixed implicit–explicit Euler scheme, consisting of two first-order schemes each applied to integrate one of the free surface conditions, is of second order in time. This fact has not been made clear in earlier work by e.g. Kim *et al.* [5].

It has been shown that the number of time steps per period needed in order to maintain stability of the BEM increases with the current strength and the order of the B-spline basis.

Also the panel aspect ratio and the current heading are important parameters. However, when the mixed Euler scheme is used on problems with weak currents, the number of time steps per period needed depends on the panel aspect ratio, but not on the current strength, current heading and the order of the basis functions. For quadratic basis functions and collinear panels and current these results agree with the findings by Vada and Nakos [14].

Finite water depth effects are shown to be insignificant for the stability of these models, except in extremely shallow water (i.e. when the water depth is smaller than a panel size).

In practical BEMs, non-uniform discretizations, truncation boundaries, and fixed or floating bodies intersecting the free surface, are used. Even though the present stability analysis does not take into account effects from such non-uniformities, they may be important for the stability behaviour of BEMs. Büchmann and Skourup [25] showed that non-uniformities in the spatial discretization may lead to instabilities, which do not vanish for $\Delta t \to 0$. Thus, the stability criteria presented in this work may be considered as necessary, but not sufficient, conditions for stability. A detailed study on the discrepancies between the stability analysis and practical BEMs is in preparation, but is considered beyond the scope of the present work.

ACKNOWLEDGMENTS

Dr Jesper Skourup is thanked for his valuable comments in the preparation of this manuscript. The people at Massachusetts Institute of Technology's Ocean Engineering Department and the Research Laboratory of Electronics have helped through many stimulating discussions on the properties of time-domain boundary element models.

APPENDIX A. FOURIER TRANSFORM DEFINITIONS AND THEOREMS

There are several ways to define the Fourier transforms of a function, so to avoid confusion, the Fourier transform definitions used in this paper and the various theorems needed are shortly stated in this appendix.

The continuous Fourier transform in space for a function $f(x, y)$ is defined as

$$\tilde{\mathscr{F}}[f] = \tilde{f}(u, v) = \int\int_{-\infty}^{\infty} f(x, y) \exp(\mathrm{i}ux + \mathrm{i}vy)\, \mathrm{d}x\, \mathrm{d}y \tag{A.1}$$

with i being the imaginary unit and $\mathscr{F}$ being chosen throughout as a symbol for a Fourier transform operator. It is often advantageous to introduce dimensionless wavenumbers based on the chosen discretization as

$$\hat{u} = \frac{u\Delta x}{2\pi}, \qquad \hat{v} = \frac{v\Delta y}{2\pi} \tag{A.2}$$

with Δx and Δy being the spatial discretization used. Thus, e.g. $\hat{u} = 0.5$ corresponds to the (spatial) Nyquist frequency in the x-direction. The principal wavenumber domain is then defined by $(\hat{u}, \hat{v}) \in [-0.5{:}0.5] \times [-0.5{:}0.5]$. In the discrete model any wavenumber outside this regime will be aliazed into the principal wavenumber regime.

The equivalent continuous Fourier transform in time is introduced as

$$\mathscr{F}[f] = \underset{\sim}{f}(\omega) = \int_{-\infty}^{\infty} f(t) \exp(-\mathrm{i}\omega t)\, \mathrm{d}t \tag{A.3}$$

such that the continuous Fourier transform in time and space can be evaluated as

$$\tilde{\mathscr{F}}[f] = \underset{\sim}{\tilde{f}}(u, v; \omega) = \iiint_{-\infty}^{\infty} f(x, y; t) \exp(\mathrm{i}ux + \mathrm{i}vy - \mathrm{i}\omega t)\, \mathrm{d}x\, \mathrm{d}y\, \mathrm{d}t \tag{A.4}$$

The discrete Fourier transform in space is introduced as

$$\hat{\mathscr{F}}[f] = \hat{f}(u, v) = \Delta x \Delta y \sum_{k,l=-\infty}^{\infty} f(k\Delta x, l\Delta y) \exp(\mathrm{i}uk\Delta x + \mathrm{i}vl\Delta y) \tag{A.5}$$

Also, the discrete Fourier transform in time, the so-called z transform, is introduced as

$$\underset{\wedge}{\mathscr{F}}[f] = \underset{\wedge}{f}(\omega) = \Delta t \sum_{k=-\infty}^{\infty} f(k\Delta t) \exp(-\mathrm{i}\omega k\Delta t) = \Delta t \sum_{k=-\infty}^{\infty} f(k\Delta t) z^{-k} \tag{A.6}$$

with

$$z = \exp(\mathrm{i}\omega\Delta t) \tag{A.7}$$

There is a convenient relationship between continuous and discrete Fourier transforms known as 'The Aliasing Theorem', stating that

$$\hat{f}(u, v) = \Delta x \Delta y \sum_{k=-\infty}^{\infty} \sum_{l=-\infty}^{\infty} \tilde{f}\left(u + \frac{2\pi k}{\Delta x},\ v + \frac{2\pi l}{\Delta y}\right) \tag{A.8}$$

The two-dimensional continuous convolution product of two functions f and g is calculated as

$$h(\mathbf{x}) = (f \otimes g)(\mathbf{x}) = \iint_{-\infty}^{\infty} f(\boldsymbol{\xi}) g(\mathbf{x} - \boldsymbol{\xi})\, \mathrm{d}\xi_1\, \mathrm{d}\xi_2 \tag{A.9}$$

with $\mathbf{x} = (x, y)$ and $\boldsymbol{\xi} = (\xi_1, \xi_2)$. The (continuous) Fourier transform of such a convolution product is easily calculated as

$$\tilde{h}(u, v) = \tilde{f}(u, v)\tilde{g}(u, v) \tag{A.10}$$

Similarly, a discrete convolution product in space (two-dimensional) can be defined as

$$h'(\mathbf{x}_i) = f * g(\mathbf{x}_i) = \Delta x \Delta y \sum_{j=-\infty}^{\infty} f(\mathbf{x}_j) g(\mathbf{x}_i - \mathbf{x}_j) \tag{A.11}$$

with the discrete Fourier transform

$$\hat{h'}(u, v) = \hat{f}(u, v)\hat{g}(u, v) \tag{A.12}$$

Also, a discrete convolution product in time (one-dimensional) is defined as

$$h''(t_i) = f \oplus g(t_i) = \Delta t \sum_{j=-\infty}^{\infty} f(t_j)g(t_i - t_j) \tag{A.13}$$

with the z transform

$$\underset{\wedge}{h''}(u, v) = \underset{\wedge}{f}(u, v)\,\underset{\wedge}{g}(u, v) \tag{A.14}$$

Continuous Fourier transforms of derivatives are calculated as, e.g.

$$\underset{\sim}{f_t} = \mathrm{i}\omega \underset{\sim}{f}, \qquad \tilde{f}_x = -\mathrm{i}u\tilde{f}, \qquad \tilde{f}_y = -\mathrm{i}v\tilde{f} \tag{A.15}$$

where the subscripts denote partial derivatives.

REFERENCES

1. Broeze J. Numerical modelling of nonlinear free surface waves with a 3D panel method. PhD thesis, University of Twente, The Netherlands, 1993.
2. Celebi MS, Kim MH, Beck RF. Fully non-linear 3-D numerical wave tank simulation. *Journal of Ship Research* 1998; **42**(1): 33–45.
3. Ferrant P. Simulation of strongly nonlinear wave generation and wave-body interactions using a 3-D MEL model. In *Proceedings of the 21st ONR Symposium on Naval Hydrodynamics*. Trondheim, Norway, 1996; 93–109.
4. Büchmann B, Skourup J, Cheung KF. Run-up on a structure due to second-order waves and a current in a numerical wave tank. *Applied Ocean Research* 1998; **20**(5): 297–308.
5. Kim Y, Kring DC, Sclavounos PD. Linear and nonlinear interactions of surface waves with bodies by a three-dimensional Rankine panel method. *Applied Ocean Research* 1997; **19**(5/6): 235–249.
6. Bunnik THJ, Hermans AJ. Stability analysis for solving the 3D unsteady free-surface condition with raised panels. In *Proceedings of the 13th International Workshop on Water Waves and Floating Bodies*. Alphen aan den Rijn, The Netherlands, 1998; 13–16 (discussions volume pp. 7–11).
7. Sierevogel LM. Time domain calculations of ship motions. PhD thesis, Delft University of Technology, The Netherlands, 1997.
8. Dommermuth DG, Yue DKP. Numerical simulation of nonlinear axisymmetrical flows with a free surface. *Journal of Fluid Mechanics* 1987; **178**: 195–219.
9. Harten A, Efrony S. A partition technique for the solution of potential flow problems by integral equation methods. *Journal of Computational Physics* 1978; **27**: 71–87.
10. Maniar HD. A three dimensional higher order panel method based on B-splines. PhD thesis, Department of Ocean Engineering, Massachusetts Institute of Technology, Cambridge, MA, 1995.
11. Kring DC. Time domain ship motions by a three-dimensional Rankine panel method. PhD thesis, Department of Ocean Engineering, Massachusetts Institute of Technology, Cambridge, MA, 1994.
12. Nakos DE. Ship wave patterns and motions by a three dimensional Rankine panel method. PhD thesis, Department of Ocean Engineering. Massachusetts Institute of Technology, Cambridge, MA, 1990.
13. Kim DJ, Kim MH. Wave–current interaction with a large three-dimensional body by THOBEM. *Journal of Ship Research* 1997; **41**(4): 273–285.
14. Vada T, Nakos DE. Time marching schemes for ship motion simulations. In *Proceedings of the 8th International Workshop on Water Waves and Floating Bodies*. St. John's, Newfoundland, Canada, 1993; 155–158.
15. Vada TK. SWAN-2, theory and numerical methods. Research Report 94-2030, Det Norske Veritas. Pages 1–30 and 72–86. Revised December, 1996.

16. Korsmeyer T, Phillips J, White J. A precorrected-FFT algorithm for accelerating surface wave problems. In *Proceedings of the 11th International Workshop on Water Waves and Floating Bodies*, Hamburg, Germany, 1996.
17. Nabors K, Phillips J, Korsmeyer FT, White J. Multipole and precorrected-FFT accelerated iterative methods for solving surface integral formulations of three-dimensional Laplace problems. In *Domain-based Parallelism and Problem Decomposition Methods in Science and Engineering*, Keyes DE, Saad Y, Truhlar DG (eds). Society for Industrial and Applied Mathematics: Philadelphia, PA, 1995; Chapter 12, 193–216.
18. de Haas P. Numerical simulation of nonlinear water waves using a panel method; domain decomposition and applications. PhD thesis, University of Twente, The Netherlands, 1997.
19. Wang P, Yao Y, Tulin MP. Wave group evolution, wave deformation, and breaking: simulations using LONGTANK, a numerical wave tank. *Internatinal Journal of Offshore and Polar Engineering* 1994; **4**(3): 200–205.
20. Piegl L, Tiller W. *The NURBS Book* (2nd edn). Springer: Berlin, 1997.
21. Schumaker LL. *Spline Functions: Basic Theory*. Wiley: New York, 1981.
22. Gradshteyn IS, Ryzhik IM. *Table of Integrals*, *Series*, *and Products* (5th edn). Academic Press: San Diego, CA, 1994.
23. Press WH, Teukolsky SA, Vetterling WT, Flannery BP. *Numerical Recipes in Fortran 77* (2nd edn). Cambridge University Press: Cambridge, U.K., 1992.
24. Anderson E, Bai Z, Bischof C, Demmel J, Dongarra J, Du Croz J, Greenbaum A, Hammarling S, McKenney A, Ostrouchov S, Sorensen D. *LAPACK Users' Guide* (2nd edn). Society for Industrial and Applied Mathematics: Philadelphia, PA, 1995.
25. Büchmann B, Skourup J. Stability of time-domain boundary element models; theory and applications. In *Proceedings of the 14th International Workshop on Water Waves and Floating Bodies*. Port Huron, Michigan, U.S.A., 1999; 13–16 (discussions in a separate volume).

